Acta Biomaterialia 147 (2022) 63–72

Contents lists available at ScienceDirect

Acta Biomaterialia

journal homepage: www.elsevier.com/locate/actbio

Full length article

Predicting and understanding arterial elasticity from key microstructural features by bidirectional deep learning

Kevin Linka[a,*], Cristina Cavinato[b], Jay D. Humphrey[b,c], Christian J. Cyron[a,d,*]

[a] Institute for Continuum and Material Mechanics, Hamburg University of Technology, Hamburg, Germany
[b] Department of Biomedical Engineering, Yale University, New Haven, CT, USA
[c] Vascular Biology and Therapeutics Program, Yale School of Medicine, New Haven, CT, USA
[d] Institute of Material Systems Modeling, Helmholtz-Zentrum Hereon, Geesthacht, Germany

ARTICLE INFO

Article history:
Received 17 January 2022
Revised 19 May 2022
Accepted 19 May 2022
Available online 25 May 2022

Keywords:
hybrid modeling
arterial tissues
explainable AI
tissue maturation

ABSTRACT

Microstructural features and mechanical properties are closely related in all soft biological tissues. Both yet exhibit considerable inter-individual differences and are affected by factors such as aging and disease and its progression. Histological analysis, modern *in situ* imaging, and biomechanical testing have deepened our understanding of these complex interrelations, yet two key questions remain: (1) Given the specific microstructure, can one predict the macroscopic mechanical properties without mechanical testing? (2) Can one quantify individual contributions of the different microstructural features to the macroscopic mechanical properties in an automated, systematic and largely unbiased way? Here we propose a bidirectional deep learning architecture to address these two questions. Our architecture uses data from standard histological analyses, two-photon microscopy and biaxial biomechanical testing. Its capabilities are demonstrated by predicting with high accuracy ($R^2 = 0.92$) the evolving mechanical properties of the murine aorta during maturation and aging. Moreover, our architecture reveals that the extracellular matrix composition and organization are the most prominent factors governing the macroscopic mechanical properties of the tissues studied herein.

Statement of significance

We present a physics-informed machine learning architecture that can predict macroscopic mechanical properties of arterial tissue with high accuracy (R2=0.92) from the tissue microstructure (characterized by imaging data). For the first time, this architecture enables also a fully automatic and largely unbiased quantification of the relevance of different microstructural features (such as collagen volume fraction and fiber straightness) for the macroscopic mechanical properties. This approach opens up unprecedented ways to predictive mechanical modeling of soft biological tissues. Moreover, it provides quantitative insights into the relation between tissue microstructure and its macroscopic properties that promise to play an important role in future tissue engineering.

1. Introduction

It is axiomatic that the microstructure of a material dictates its macroscopic mechanical properties, yet such a prediction has remained elusive. In biomechanics, there is a particular need to understand the link between the microstructure of a soft tissue and its macroscopic mechanical properties [1–6]. Once such links have been understood, it may be possible for advances in biomedical imaging to be used as a non-invasive tool to determine patient-specific biomechanical properties, with effective tissue characterization [7] promising to pave the way toward improved diagnosis and thus patient care. Moreover, understanding this link will reveal better the microstructural origin of macromechanical tissue functionality [8], which is of major importance in many fields including tissue engineering. Finally, understanding the link between microstructure and macromechanical properties in soft tissue may enable one not only to estimate current mechanical properties but also to predict and understand changes due to aging or progressive diseases. This approach could thus improve risk stratification

* Corresponding authors.
E-mail address: christian.cyron@hereon.de (C.J. Cyron).

https://doi.org/10.1016/j.actbio.2022.05.039

by forecasting the tissue evolution [9,10], and in the long run help to develop ways to counteract unfavorable changes.

Unraveling the complex interplay between the multi-layer composite structure of the aortic wall and its mechanical response to hemodynamic loading remains among the major unsolved problems in vascular biomechanics. Histological assessments and two photon-microscopic examinations have provided plentiful and increasingly accurate insights into the microstructure of soft biological tissues over the last decade [11–19], as revealed in part by papers aimed at using these insights to model macroscopic mechanical properties [19–24]. However, while the constitutive models presented in these papers succeeded in capturing the observed mechanical behavior by parameter fitting, they have so far been unable to predict this behavior from given microstructural data. In addition, our quantitative understanding of the importance of the different microstructural characteristics (descriptors) to the macromechanical properties remains limited. The complexity of the relationship between microstructure and macroscopic properties of soft tissue arises in part from the continual changes the vascular wall undergoes due to growth and remodeling. Following rapid changes in the early postnatal period, cells gradually stabilize their phenotype during the period of late maturation, along with blood flow, blood pressure and axial stretch, leading to a largely constant overall collagen and elastin mass in adulthood [16,25,26]. Although its overall mass remains largely constant, collagen turns over continuously in adulthood on the time scale of months. By contrast, elastin deposited primarily in the perinatal period slowly degrades, having a half-life on the order of decades. Thus, during natural aging, elastin predictably undergoes degradation and fragmentation and is increasingly replaced by an increasing amount of load-bearing collagen, overall manifesting in increased aortic stiffness [27,28]. The complexity of this continuous interplay between structure and function further increases if we consider subject-to-subject differences [15,16,19,20,29,30]. Appropriately, some have tried to link microstructure to macromechanical properties albeit by conventional methods such as linear or standard nonlinear regression [16,31–33].

Over recent years, machine learning has risen as a powerful tool to study complex behaviors of materials like plasticity [34] or nonlinear anisotropic elasticity [35]. To reduce the amount of training data required - which is particularly important in biomedical engineering where data collection is typically associated with a substantial cost per sample - physics-informed machine learning, often also referred to as hybrid modeling or grey-box modeling, has attracted increasing attention [36–39]. Recently, it has been shown that this concept can provide important insights into arterial mechanics [40].

In this study, we propose a physics-informed bidirectional deep learning architecture. Using data from standard histological analyses, two-photon microscopy and biaxial biomechanical testing, this architecture can learn to predict the macromechanical properties of murine arterial tissue from available microstructural features. Moreover, after applying a so-called relevance propagation [41] to the already trained deep neural network, this approach reveals and ranks the importance of the different microstructural features to the macromechanical tissue properties in a fully automated and largely bias-free way. Applying our machine learning architecture to murine tissue at different ages of the mice yields important insights into the evolving role of the different constituents of the tissue during maturation.

2. Experimental data

A major challenge in predictive biomechanical modeling is ensuring high accuracy over a broad range of different tissue microstructures, arising due to natural or pathological tissue remodeling processes. Therefore, it is vital to train the model with data representing a variety of different tissue microstructures. Here, we employed data from murine tissue samples at five different ages from weaning to one year of natural aging.

2.1. Tissue preparation and testing

The samples were harvested from the descending thoracic aorta and mechanically tested under *in vivo* equivalent loading conditions [16]. In total, we used 25 samples from female C57BL/6 mice at postnatal ages of P21 ($n = 9$), P42 ($n = 4$), P98 ($n = 4$), P230 ($n = 4$), P365 ($n = 4$). The higher pooling density of samples from the P21 group helps to improve machine learning at the lower age limit, given that the microstructure in P21 samples not only differs significantly from all remaining groups, it is also the most dynamic [16]. All animal procedures were approved by the Institutional Animal Care and Use Committee (IACUC) of Yale University. Consistent with well-established protocols [31], each mouse was euthanized by intraperitoneal injection of Beuthanasia-D and the segment of descending thoracic aorta between the first and the fourth pairs of intercostal branches was excised and minimally handled with the aim of removing perivascular tissue and ligating branches. Specimens were then secured on micro-cannulae within a computer-controlled biaxial device at room temperature in Hank's buffered physiologic solution. Passive testing was performed after a consistent passive preconditioning via four distension cycles from 10 mmHg to the age-specific maximum luminal pressure (P21: 100 mmHg, P42: 120 mmHg, P98, P230, P365: 140 mmHg) at the specimen-specific preferred *in vivo* axial stretch. Three cyclic pressure-diameter protocols at specimen-specific fixed axial stretches (from -5% to +5% of the specimen-specific *in vivo* value; see Table S5) and four cyclic axial force-length protocols at different fixed pressures (10 mmHg to maximum pressure for each age) were applied. Computer-controlled sub-micron resolution micro-stepper motors provided the cyclic axial motions while a computer-controlled pump controlled the pressurization; a high-resolution video microscope measured the diameter in the central region, standard force and pressure trasducers measured the applied biaxial loads, and a stepper motor encoder measured length changes [31]. Following mechanical testing, the aortic sample was maintained at the specimen-specific axial stretch and a fixed pressure equivalent to the age-specific diastolic luminal pressure (P21: 50 mmHg, P42, P98, P230, P365: 80 mmHg) based on *in vivo* blood pressure measurements in age-matched mice previously reported [25,26]. The water immersion 20X objective of a LaVision Biotec TrimScope Two-Photon microscope, equipped with a Titanium-Sapphire Laser (Chameleon Vision II, Coherent) tuned at 840 nm, was centered over the sample. Second harmonic generation of collagen (390-425 nm), autofluorescence of elastin (500-550 nm), and fluorescence of cell nuclei (with cell-permeant SYTO 17 red fluorescent stain, over 550 nm) were detected simultaneously in a region of 500 μm x 500 μm x 100 μm (respectively, in axial, circumferential and radial axes of the sample) in the form of three-dimensional images. Such acquisition was performed twice, on the dorsal side and on the ventral side of each aorta, while maintaining the specimen-specific axial stretch and the pressure equivalent to the age-specific diastolic luminal pressure. For further detail on the microstructural acquisition please refer to [16].

2.2. Mechanical data

From collected passive biaxial mechanical data (Fig. 1), i.e., luminal pressure, axial force, outer diameter, and axial stretch, recall that the mean Cauchy stress across the wall of a thin-walled ($a \gg h$) or residually stressed vessel loaded by an internal pressure and axial force can be written in the form of circumferential and

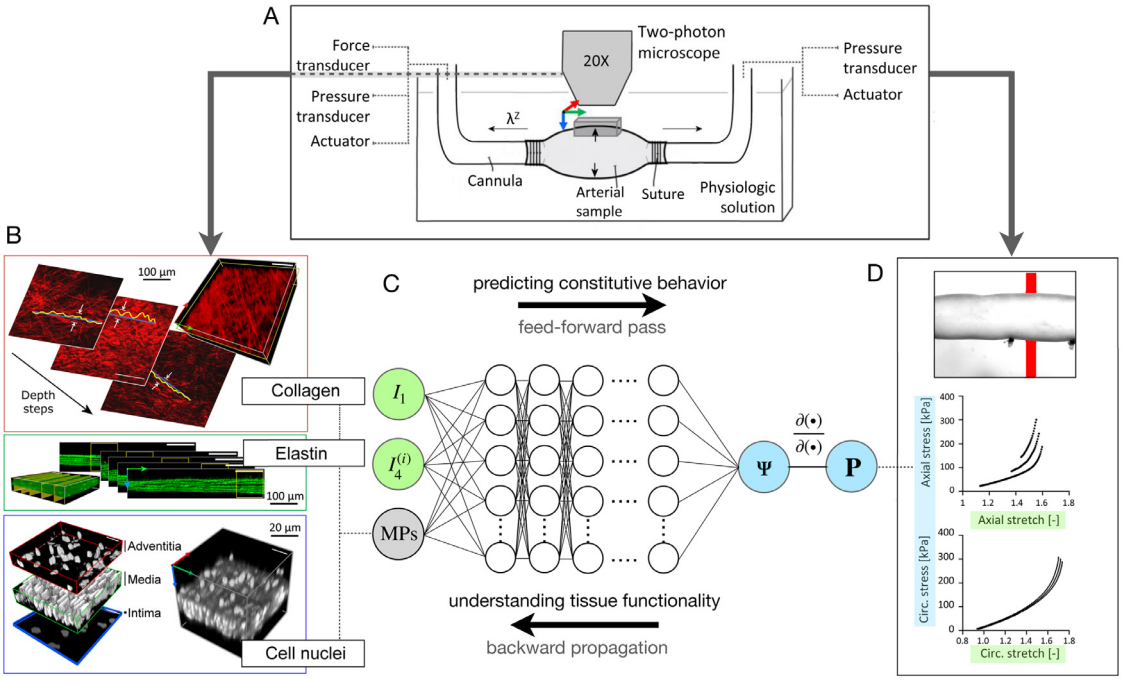

Fig. 1. Flowchart of the data-driven bidirectional deep learning architecture: (A-B) coordinate invariant measures of the deformation (I_1, $I_4^{(i)}$) and microstructural parameters (MPs) from two-photon imaging are provided as input for a (C) constitutive artificial neural network (CANN) whose output is strain energy (Ψ), from which stresses derive. To train the CANN, stress values obtained from (D) a large number of biaxial biomechanical distension-extension data are provided to the CANN as reference output. Once the CANN has been trained, an additional backward propagation step is performed that quantifies the relevance of the different input features for the mechanical properties of the tissue. Note that the video-microscope for measuring outer diameter on-line is not shown, but is placed orthogonal to the axis of the multiphoton microscope.

axial components [42]:

$$\sigma_{\theta\theta} = \frac{Pa}{h}, \quad \sigma_{zz} = \frac{f_T + \pi a^2 P}{\pi h(2a+h)} \tag{1}$$

where P is the luminal pressure, a the deformed inner radius, h the deformed thickness, and f_T the applied axial force measured by a force transducer. Note that a and h were calculated, assuming incompressibility, using the unloaded volume of the vessel, the instantaneous axial length and the deformed outer radius.

2.3. Microstructural data

Microstructural metrics were derived from 3D microstructural images of the samples acquired at *ex vivo* equivalent age-specific diastolic loading conditions throughout two primary (medial and adventitial) layers of the aortic wall. In total, they include 16 tissue descriptors, total wall thickness and the relative adventitia:media ratio plus 14 microstructural parameters: adventitial collagen volume fraction [VF], adventitial elastin VF, adventitial cell nuclei VF, medial collagen VF, medial elastin VF, medial cell nuclei VF, collagen fiber straightness, collagen fiber bundle width, preferred collagen fiber orientation, collagen fiber concentration in the preferred fiber orientation (defined below), inter-lamellar distance in the medial elastic lamellae, density of smooth muscle cells, density of fibroblasts and density of endothelial cells. For a detailed description of the assessment of these parameters, see [16]. In brief, layer-specific thickness was quantified by measuring the mean intensity profiles along the radial direction for multiple volume subunits of the 3D images and automatically thresholding the two tails of the normalized intensity profile corresponding to defined thresholds to delimit the internal and external limits of the wall. The interface between the adventitia and media was defined as the radial position of the maximum derivative of the intensity profile of the nucleus signal between the radial position of the maximum of the collagen intensity profile and the inner limit of the wall. Component volume fractions (VFs) within the adventitia and media were defined after binarization of the images as black and white pixel ratios between the specific limits of each layer measured previously for each volume subunit. Values of volume fraction were taken as averages of the subunit's values of each 3D image. Note that the total volume used to define the VF was a relative sum of fibrillar collagen, elastin, and nuclei and does not consider other components (e.g., cytoplasm, non-fibrillar collagen and GAGs). The description of the collagen fiber bundles focused on in-plane (i.e., axial-circumferential plane of the artery) parameters: straightness, bundle width, and orientation distribution. Straightness was computed as the ratio of end-to-end to total fiber length for fibers consistently selected at multiple positions. Bundle width was measured as the transversal section of multiple bundles of fibers in the axial-circumferential plane. Orientation distributions were estimated for each circumferential-axial section of the adventitial volume using a 2D structure tensor analysis, OrientationJ plug-in for ImageJ. All in-plane orientation distributions were averaged along the radial direction and normalized, and the resulting mean orientation distribution was reported between ±90° (circumferential direction), with 0° defining the axial direction of the arterial sample. Distributions were parameterized with a Von Mises circular probability density function

$$F(\theta|\mu,\kappa) = \frac{\exp\{\kappa\ \cos(\theta-\mu)\}}{2\pi\, I_0(\kappa)} \tag{2}$$

where μ is the preferred orientation, I_0 a modified Bessel function, and κ a measure of concentration [43] that quantifies fiber alignment at the tissue level. Layer-specific cell densities were calculated as the number of cells per unit volume by counting the number of nuclei within defined sub-volumes of the 3D image and normalizing by the appropriate sample- and layer-specific thickness. All investigated experimental data are represented graphically in Fig. 2 and listed in Tables S1-S4. While the preferred collagen orientation and associated fiber alignment were used to determine

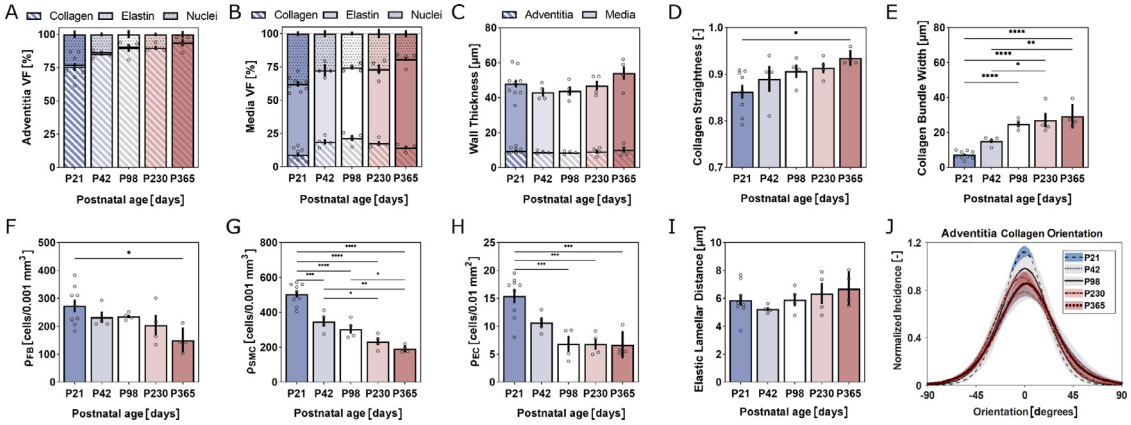

Fig. 2. (A-I) Overview of microstructural descriptors measured experimentally as a function of the age and used in the present study. (J) The adventitial collagen orientation is represented as the mean in-plane orientation distribution as a function of the angle of the collagen fibers, from ±90° (circumferential direction of the artery) to 0° (axial direction of the artery). The abbreviation VF denotes volume fraction. Overbars indicate statistical significance between the age groups, where * $p < 0.05$, ** $p < 0.01$ and *** $p < 0.001$.

the invariants describing the collagen microstructure (*SI Appendix*), all remaining microstructural parameters were direct inputs to the machine learning architecture (Fig. 1).

2.4. Statistics

Statistical differences in microstructural parameters among all age groups (each value was the average of dorsal and ventral values) were assessed using a non-parametric Kruskal Wallis test followed by Dunn's multiple comparison test. Normality was checked via a Shapiro-Wilk normality test. For all reported comparisons, $p < 0.05$ was considered significant, with one-to-three asterisks denoting p values lower than 0.05, 0.01 and 0.001, respectively.

3. Machine learning

3.1. Constitutive artificial neural network (CANN)

The machine learning architecture used herein is illustrated in Fig. 1. It consists of a so-called CANN, a recently developed type of physics-informed deep neural network that is particularly suitable for learning the constitutive behavior of mechanical materials and their dependence on microstructural features [35]. CANNs are based on a multi-layer neural network. Compared to classical statistical regression models, neural networks have the advantage that they can handle in a straightforward and simple way large and complex functional spaces, they can incorporate tailor-made prior knowledge, and they can include differential operators among other advantages. The CANN receives as input the current tissue strain (defined in terms of strain invariants) as well as the following 14 microstructural parameters: wall thickness, the adventitial thickness fraction, layer-specific (adventitial and medial) collagen, elastin and cell nuclei volume fractions, collagen straightness, collagen bundle width, elastin interlamellar distance, fibroblast density, endothelial cell density and smooth muscle cell density. Our objective is to train the CANN to predict from this information the mechanical stress to which the tissue is subjected at a given strain, noting that the relation between tissue strain and stress defines its macromechanical properties. To train the CANN by supervised machine learning, it has to be provided as training data many samples where for each input (tissue strain and microstructure) the correct output (tissue stress) is given. To operate our particular CANNs, one has to define a set of strain invariants (or at least the total number of such strain invariants) which is sufficient to describe the considered deformation. Here, this invariant set needs to account for the incompressible and anisotropic nature of arterial tissue. Following the well established Gasser-Ogden-Holzapfel (GOH) model for describing the non-linear elasticity of aortic tissue [44], we consider invariants of the type

$$I_1 = \mathrm{tr}(\mathbf{C}), \quad I_4^{(i)} = \mathbf{C} : \mathbf{M}_i \otimes \mathbf{M}_i \tag{3}$$

with $i = 1, 2$ denoting preferred directions, $\mathbf{C}$ the right Cauchy-Green deformation tensor, and $\mathbf{M}_i = \sin\alpha_i \mathbf{e}_z + \cos\alpha_i \mathbf{e}_\theta$ unit vectors in the preferred directions in a suitable reference configuration. The first strain invariant I_1 accounts for the amorphous matrix and the two invariants $I_4^{(1)}$ and $I_4^{(2)}$ express the stretch squared in the two preferred collagen fiber directions $I_4^{(i)} = \lambda_\theta^2 \sin^2\alpha_i + \lambda_z^2 \cos^2\alpha_i$ with the circumferential stretch λ_θ, axial stretch λ_z and the associated two mean fiber orientations $\alpha_1 = \alpha$ and $\alpha_2 = -\alpha$. In addition to the invariant basis of the GOH model, we also tested one other widely used constitutive model for arterial tissue that is often referred to as a four-fiber model (4FF) [45]. Compared to the GOH model, the 4FF model complements the invariant basis by two more invariants $I_4^{(3)}$ and $I_4^{(4)}$ expressing support in the axial ($\alpha_3 = 0$) and circumferential ($\alpha_4 = \pi/2$) tissue directions, which is motivated not only by actual fiber directions but also the seldom quantified effects of cross-links. Both for the GOH and the 4FF model, the strain energy function comprising an isotropic contribution Ψ_{iso} and an anisotropic contribution Ψ_{aniso} can generally be written as

$$\Psi = \Psi_{\mathrm{iso}}(I_1) + \sum_{i=1}^{N} \Psi_{\mathrm{aniso},i}\left(I_4^{(i)}\right), \tag{4}$$

where $N = 2$ for the GOH model and $N = 4$ for the 4FF model. For more details of the GOH and 4FF model see *SI Appendix*.

As illustrated in Fig. 1, the functional relation between a certain set of invariants and the strain energy Ψ is approximated in CANNs by a deep neural network [35]. To further compute the second Piola-Kirchhoff stress tensor $\mathbf{S}$, CANNs evaluate the analytical equation

$$\mathbf{S} = 2\left(\frac{\partial \Psi}{\partial I_1}\mathbf{I} + \sum_{i=1,2} \frac{\partial \Psi}{\partial I_4^{(i)}} \mathbf{M}_i \otimes \mathbf{M}_i\right) - p\mathbf{C}^{-1}, \tag{5}$$

by symbol-to-symbol automatic differentiation. Here, p denotes a Lagrange multiplier (pressure-like term) to enforce incompressibility. The first Piola-Kirchhoff stress tensor $\mathbf{P}$ can then be computed by the well-known relation $\mathbf{P} = \mathbf{FS}$. Altogether, the CANNs receive as input strain invariants and information about the microstructure of the tissue. Their output is the strain energy density function

Ψ and the associated stress. Provided sufficient strain-stress data and microstructural data, the CANNs are able to learn to predict for a material sample with a given microstructure in a given strain state the resulting strain energy and stress. That is, they can learn to predict the constitutive relation between stress and strain from available microstructural information. Note that the GOH model requires two microstructural parameters to define the generalized invariants (i.e., fiber dispersion parameter κ_{col} and the preferred fiber orientation α) and the 4FF-model only one, the preferred fiber orientation for the symmetric diagonal families. Nevertheless, we used the 14 tissue descriptors listed above for all machine learning architectures, i.e., architectures relying on the invariant basis of the GOH and 4FF models, which is defined to allow for a high comparability between the different employed machine learning architectures.

3.2. Model training and hyperparameter tuning

To train our CANNs, we used Adam optimization [46] for minimizing the mean-squared-error (MSE) loss function

$$\text{MSE} = \sum_i |\text{P}^i_{zz} - \text{P}^i_{\text{exp},zz}|^2 + \sum_j |\text{P}^j_{\theta\theta} - \text{P}^j_{\text{exp},\theta\theta}|^2. \tag{6}$$

Here, P^i_{zz} and $\text{P}^j_{\theta\theta}$ are the axial and circumferential components of the first Piola-Kirchhoff stress as computed by our CANNs, while P^i_{exp} are the corresponding experimentally calculated values. The indices i, j loop through all experimentally collected stretch-stress tuples included in the training process. The deep neural networks are trained by a leave-one-out cross validation (LOO-CV) scheme. Thereby, one sample is retained for validation (i.e., the model prediction) in each fold and another one as a test sample to trigger early stopping of the machine learning (to avoid overfitting). The test samples were always chosen from the same age group as the validation sample to ensure that both microstructures were similar enough to make the test sample a good good basis to trigger early stopping. Our whole framework was implemented in Keras with TensorFlow backend [47,48]. More details on training and validation are provided in the *SI Appendix*.

3.3. Layer-wise relevance propagation

To analyze the individual relevance of the microstructural features for the macroscopic mechanical properties, we applied a so-called layer-wise relevance propagation (LRP) [41], a method from the field of explainable artificial intelligence. Here, we used LRP i) to rank the model parameters according to their contribution to the macromechanical properties of the tissue and ii) to identify reduced subsets of highly relevant features, which are sufficient to ensure high predictive accuracy. Thereby, LRP propagates the predictions of the trained network backwards into the network to determine the relevance of each input feature for the network output, using a set of defined propagation rules. Technically, the relevance scores in LRP are computed as follows. Consider a network layer with neurons k and its preceeding layer with neurons j. Assume that the relevance score for all neurons k is already known as R_k. Then the relevance scores R_j of the neurons in the preceeding layer can be defined as

$$R_j = \sum_k \frac{z_{jk}}{\sum_j z_{jk}} R_k, \tag{7}$$

where $z_{jk} = a_j w_{jk}$ with the network weights w_{jk} connecting the neuron j and k and the activation a_j of neuron j. The denominator ensures a conservation property. Due to the positivity of the strain energy function, we used a slightly modified version of (7) favoring the effect of positive over negative contributions by

$$R_j = \sum_k \left(\alpha \frac{(a_j w_{jk})^+}{\sum_{0,j} (a_j w_{jk})^+} - \beta \frac{(a_j w_{jk})^-}{\sum_{0,j} (a_j w_{jk})^-} \right) R_k, \tag{8}$$

which divides the paramters z_{jk} into positive and negative ones using the operators $(\bullet)^+ = \max(0, \bullet)$ and $(\bullet)^- = \min(0, \bullet)$. The positive and negative contributions were weighted differently by α and β. Herein, we used $\alpha = 2$ and $\beta = -1$, observing the conversation property $1 = \alpha + \beta$. Note that in (8) the sum includes all values of j as well as 0 with $a_0 = 1$ to introduce an extra neuron w_{0k} representing the neuron bias.

4. Results

4.1. Prediction of mechanical properties from microstructure

Our trained physics-informed machine learning architecture predicted well the constitutive behavior (i.e., the relation between stress and strain) of murine aortic tissue from given microstructural features. The best model performance was obtained by informing a deep neural network model with the invariant basis of the 4FF model and without any normalization of the 14 scalar feature inputs. To train and validate the deep neural networks, we apply age-specific leave-one-out cross validation (LOO-CV), as detailed above. Our trained grey-box model managed to predict the constitutive behavior throughout all five ages with a median coefficient of determination of $R^2 = 0.92$. Representative predicted stress-strain curves together with the underlying learning history are depicted in Fig. 3 for the five age groups considered. Fig. 4A provides an overview of the accuracy achieved separately in the different age groups. Though model accuracy is best in the three central age groups, P42 [$R^2 = 0.94$ (95% CI: 0.87-0.96)], P98 [$R^2 = 0.91$ (95% CI: 0.88-0.93)] and P230 [$R^2 = 0.93$ (95% CI: 0.69-0.94)]), also in the youngest group, P21 [$R^2 = 0.9$ (95% CI: 0.79-0.91)], and the oldest group, P365 [$R^2 = 0.93$ (95% CI: 0.65-0.94)] the predicted accuracy still had a median $R^2 \geq 0.9$, see also Fig. S1. Note that the model does not receive age as an input parameter and thus does not explicitly predict any age-specific tissue responses. Rather it is capable of dealing with age-dependent change of the tissue elasticity implicitly on the basis of the age-dependent changes of the microstructure. In total, only two outliers are observed, one in the P230 and another one in the P365 group. In Fig. 4B, we additionally quantify for each sample the Euclidean distance of the vector containing all its microstructural descriptors as elements (e.g., collagen volume fraction, collagen straightness) from the associated median. As expected, the general trend of the Euclidean distances shows raising tails towards both age limits and is low to moderate between. Furthermore, Fig. 4C highlights for each sample the microstructural descriptors that fall into the 95th (red) and 5th (blue) percentile of the interval in which this descriptor ranges. The number of such descriptor outliers is listed for each sample in Fig. 4D. Remarkably, all three samples (P21-7, P230-2, P365-2) for which a poor predictive accuracy is observed ($R^2 < 0.7$) exhibited at least one outlier for one of the descriptors found below to be highly relevant for model prediction. Further details about the validation scheme and the measure of accuracy used in our machine learning procedure are outlined in *SI Appendix*.

4.2. Relevance of microstructural features

We used layer-wise relevance propagation (LRP) to study the specific influence of the microstructural descriptors forming the input to our neural network. For our LRP, we relied on a network trained with descriptors subjected individually to a min-max

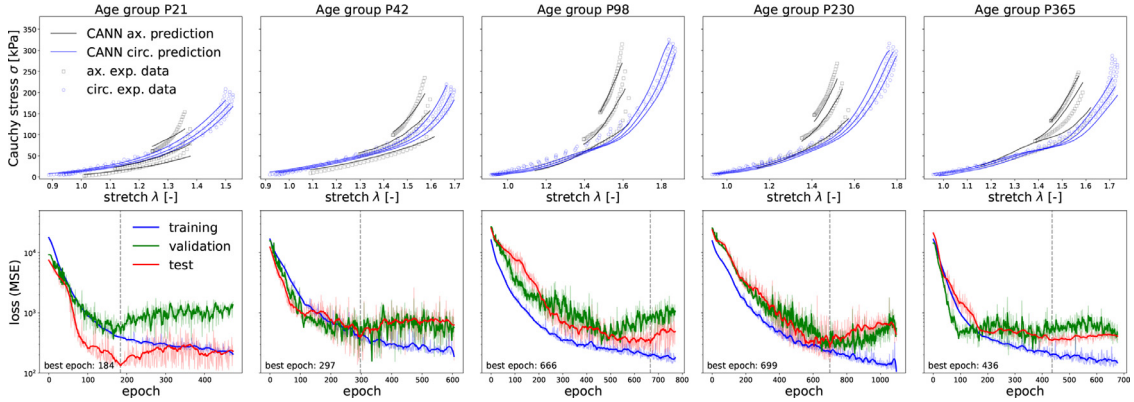

Fig. 3. The top row shows measured (symbols) and predicted (solid lines) biaxial stress-stretch relations for one representative validation sample for each of the five age groups (postnatal days P21, P48, P98, P320 and P365), showing both axial (ax.) and circumferential (circ.) responses for a few of the 7 different mechanical testing protocols. The bottom row presents the associated decrease of the loss function (mean-square error) of the model over the training epochs for the training data, test data and validation data. To prevent overfitting, the training was considered complete (early stopping marked by vertical dashed lines) when the loss function of the test sample (not included in the training data) started to increase.

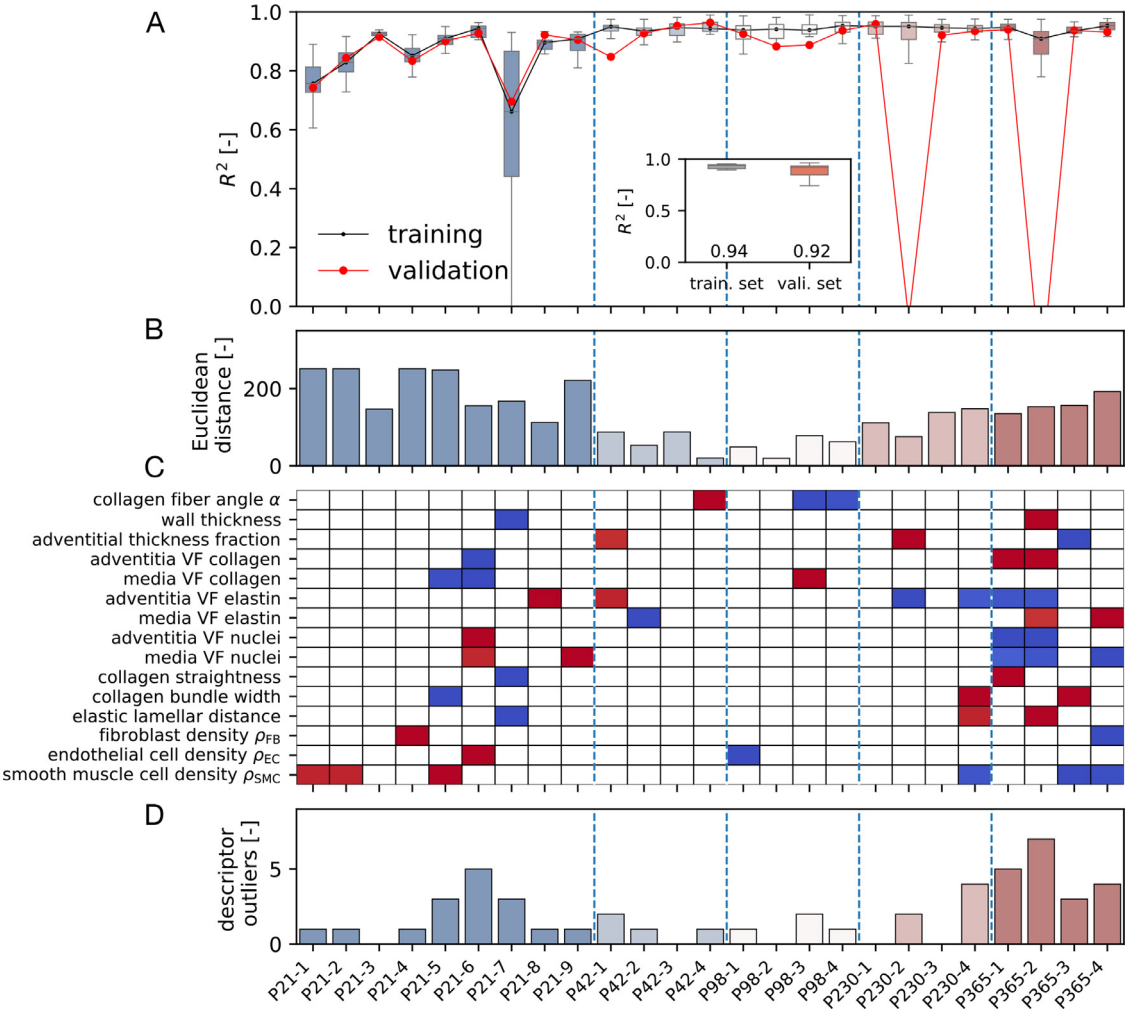

Fig. 4. Overview of predictions of the CANNs for the four-fiber family (4FF) invariant basis. (A) R^2 accuracy of trained CANN for each sample (median value of all training folds and R^2 accuracy if a sample was selected as a validation sample). (B) The Euclidean distance of the individual sample feature to the median feature space. (C) Summary of all employed inputs with red boxes indicating that the associated microstructural parameter is above the 95th percentile and blue boxes highlighting a parameter that is below the 5th percentile. (D) Total amount of features above the 95th or below the 5th percentile for each specific sample at a different postnatal age, P21 to P365. VF is volume fraction. For an overview of the predictions of the CANNs for the Gasser-Ogden-Holzapfel (GOH) invariant basis see also Fig. S2. Sample accuracy with a $R^2 \leq 0$ are: P230-3 = -0.02 and P-365-2=-0.14.

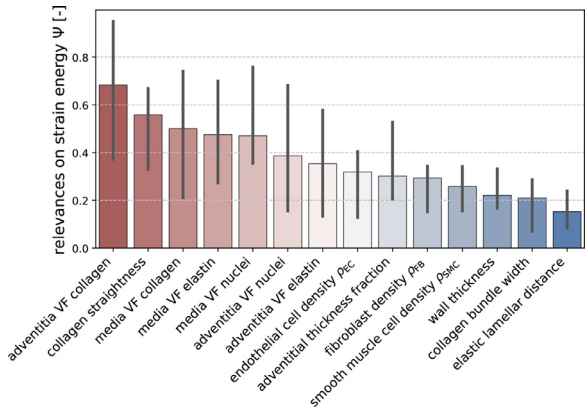

Fig. 5. Ordered relevance of different microstructural descriptors for macroscopic strain energy Ψ (median relevance scores across all samples including the 95% confidence interval). VF is volume fraction, ρ is cell density, the subscripts EC, FB and SMC subscripts are endothelial cells, fibroblasts and smooth muscle cells, respectively.

normalization. This helped to avoid a biased weighting of specific descriptors in the LRP. The training procedure preparing the LRP again relied on a LOO-CV, providing as many trained models as tissue samples. We applied LRP separately to each of these models and report in Fig. 5 median relevance scores.

The highest relevance was observed for the adventitial collagen volume fraction, followed in descending order by collagen fiber straightness, the medial collagen volume fraction, the medial elastin volume fraction, medial nuclei volume fraction and adventitial elastin volume fraction. Thus, 6 out of the 7 microstructural parameters most relevant to the macro-mechanical properties are (layer-wise) volume fractions of the different tissue constituents.

Based on the relevance scores in Fig. 5, we studied possible predictions of the macroscopic mechanical properties by a reduced set of microstructural descriptors. To this end, we trained a model with only the most relevant 7 out of the 14 available descriptors as input. We found that this model still achieved a predictive accuracy of $R^2 = 0.9$ on the validation set (Fig. S5). In addition, to understand the importance of layer-resolved vs. layer-averaged information, we repeated model training with only a set of 4 microstructural input parameters. In this case, the volume fractions for medial and adventitial collagen, elastin and nuclei were averaged over the media and adventitia. Additionally, the collagen straightness was provided, which also belongs to the 7 most relevant input parameters identified initially. Interestingly, even this strongly reduced input space of only four parameters allowed us to train a model that achieved a mean prediction accuracy of $R^2 = 0.85$ (Fig. S6).

4.3. Age-related microstructural relevance

Tissue maturation and aging associate with long-term tissue remodeling processes and thus changes in tissue microstructure and functionality. They can be expected to affect also the relevance of the different microstructural properties of the tissue. To understand this process, we revisited the results of the aforementioned LRP analysis. This time, we studied not the median relevances across all samples but rather the ones across the five different age groups. We found four significant monotonic relationships (Spearman's rank correlation coefficient $\rho \geq 0.9$ and $p < 0.001$). The adventitial collagen volume fraction and collagen straightness correlated positively with age. By contrast, a negative correlation emerged for smooth muscle cell density and the thickness fraction of adventitia and media, shown in Fig. 6. Interestingly, the two descriptors that correlate positively with age are also the ones

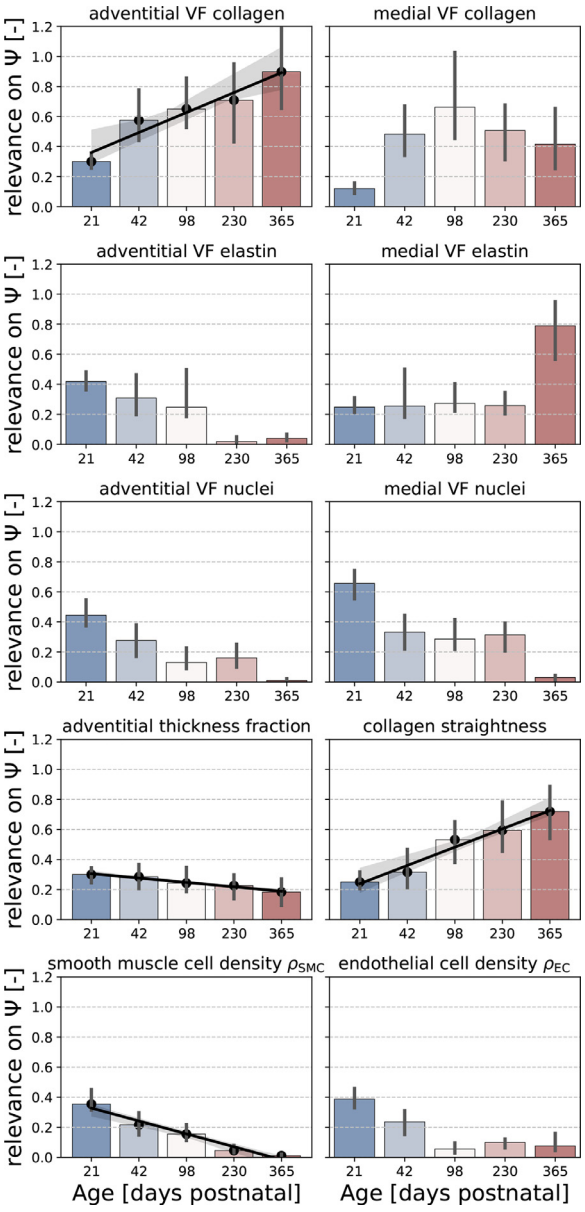

Fig. 6. Age dependent relevance scores of microstructural parameters for significant monotonic relationships. Bars indicate the median values, errorbars the 95% confidence interval and the shaded areas the standard deviation. VF is volume fraction, ρ is cell density. Relevance scores of all 14 available features can be found in Fig. S7.

with the highest overall relevance in Fig. 5. Furthermore, we considered the relevance vs. age relationship for microstructural features with an age group-specific relevance heuristically defined as above 0.4. These scores show a common trend among microstructural parameters for some ages more than others. Regarding the collagen, the score is above the threshold and monotonically increasing for adventitial collagen volume fraction from age P42 and collagen straightness from age P98, which is above the threshold for medial collagen volume fraction from age P42 but with a peak at P98. Cell-related parameters show instead a very different trend, with relevance above the threshold for nuclei volume fraction in the media and adventitia at P21, as well as densities of endothelial cells, smooth muscle cells and fibroblasts high at P21 (although lower than the chosen threshold) but decreasing afterwards. Is is noted that the development of the aorta is characterized by a transition from a near cell-only wall in late gestation and early postnatal to a gradually more balanced distribution of cells and extracel-

lular matrix [26]. When elastin is considered, the relevance score largely exceeds the threshold for medial elastin volume fraction at P365 and is marginally over the threshold for adventitial elastin volume fraction at P21. Here discussed relevance scores in dependency of sample age are shown in Fig. 6, while all relevance scores can be found in Fig. S7.

4.4. Effect of prior information

Fig. 4 also shows the results obtained with a CANN based on the invariant basis of the 4FF model. We also tested a CANN based on the invariance basis of the GOH model, which revealed a similar (though slightly worse) performance ($R^2 = 0.89$ vs. $R^2 = 0.92$, cf. Fig. S2). CANNs contain general prior information from materials theory. Moreover, the two CANN architectures tested herein contain some limited additional prior information about the invariant basis that can be used to describe soft tissue elasticity. Nevertheless, both CANN architectures contain substantially less prior information than the GOH model or the 4FF model as a whole because these two models not only define a certain invariant basis but also the specific functional relation connecting the invariants in the calculation of the strain energy Ψ. To study the effect of prior information, we thus tested two additional machine learning architectures, where the functional relation defining Ψ was not learned from the given data by a CANN but instead included via the full functional relations for Ψ given by the GOH and 4FF models (cf. *SI Appendix*) which thus learned only the free material parameters within these models from the given data. Clearly, this introduces much more prior information than just the invariant bases of these models. Interestingly, the CANN-based approach performed in both cases much better ($R^2 = 0.89$ and $R^2 = 0.92$) than the latter approach using the full GOH and 4FF model ($R^2 = 0.73$ and $R^2 = 0.74$), cf. Figs. S3 & S4.

5. Discussion

Herein, we have introduced a novel physics-informed bidirectional deep neural network that combines microstructural data from two-photon microscopy and biomechanical testing data to predict the macroscopic stress-strain behavior of arterial tissue with an unprecedented accuracy ($R^2 = 0.92$) given a relatively small data base ($n = 25$ samples). To this end, our neural network employes 14 distinct tissue features characterizing the tissue microstructure and biaxial data from seven cyclic protocols reflecting the macromechanical properties. We demonstrate that beyond training highly predictive tissue models, we could identify the individual microstructural parameter relevance to the learned strain energy functions using layer-wise relevance propagation (LRP). Compared to [40], we achieved in this study a much higher predictive accuracy, presumably due to four important improvements in our approach: first, whereas [40] mainly uses raw imaging data, we preprocessed the imaging data to compute 14 physiologically relevant microstructural features provided to our neural network as individual input variables, endowing our training data with substantial prior knowledge about the physiological relevance of specific features in the imaging data; second, we used in vivo equivalent biaxial mechanical testing data rather than the uniaxial data on which [40] relied and which do not capture the full complexity of anisotropic arterial elasticity; third, by using tissue from an inbred strain of mice, we confined our focus to tissue samples with a lower microstructural variability, resulting for the same number of training samples in a denser sampling of the relevant latent space and thus more accurate predictions; fourth, we used CANNs rather than a pre-defined functional relation to learn the strain energy function, which helped to reduce adverse a priori biases in our learning architecture.

Using LRP we were able to quantify the relevance of these 14 descriptors for the predictions of the trained neural network. It turned out that 6 among the 7 most important descriptors were volume fractions of different tissue constituents, the 7th being the collagen fiber straightness. These findings are in good agreement with widely used constitutive models of soft biological tissues, which often use constituent volume fractions and the so-called recruitment stretch (a measure of fiber straightness in the in vivo configuration) as major governing model parameters [49–53]. Results of our LRP further enabled us to define reduced sets of 7 or even only 5 key microstructural features that enabled predictions of a nearly comparable quality ($R^2 = 0.9$ and $R^2 = 0.85$). Therefore, LRP not only helps one to quantify in an automated and largely unbiased way the role of different features of the microstructure, it can also aid in the development of new efficient protocols for microstructural analysis that can focus measurement on the most relevant features.

We also compared the performance of four different physics-informed machine learning architectures. Two used well-established constitutive models for arteries (the GOH and the 4FF model) and only learned the material parameters within these models from the given data. By contrast, the other two models used only the invariant bases of the same two well-established constitutive models, leaving the functional dependence of the strain energy on the invariants to be learned by two distinct CANN models from the data. Interestingly, a higher predictive accuracy emerged for the latter two models ($R^2 = 0.89$ and $R^2 = 0.92$) compared to the former two models ($R^2 = 0.73$ and $R^2 = 0.74$). At first glance this is surprising because results of machine learning are generally expected to improve with the addition of more prior information. Our results thus suggest that for the specific tissue samples studied herein, both the GOH and the 4FF model may depend on a proper invariant basis (which explains the excellent performance of the associated CANNs) but the specific functional dependence of the strain energy on these invariants is not ideal. Indeed, this is not surprising for the assumed additivity of the isotropic and anisotropic contributions disregards, in principle, interactions between the matrix and embedded fibrous constituents, something shown previously to be important in another soft tissue [54,55]. Moreover, the GOH and 4FF models describe phenomenologically the stiffening due to collagen fiber straightening under tension, not via a more microstructurally motivated approach [56], though many such approaches also tend not to model the true complexity of fibrillar collagens, including their interactions with minor collagens and critical proteoglycans, both aggregating and small leucine rich.

Toward this end, we are reminded that all phenomenological models, including GOH and 4FF, are designed to describe macroscopically measured mechanical behaviors, which they can do well, but they are not designed to capture precisely the underlying microstructural basis, which ultimately includes contributions from actual constituents as well as constituent-to-constituent interactions and copius cross-links. In the absence of the requisite microstructural detail and theoretical advances in this regard, physics-informed neural networks offer an advantage depending on the application of interest. In addition to the mentioned model-specific limitations, classes of fiber-reinforced hyperelastic materials can be prone to unexpected responses (e.g. transversal expansions under uniaxial tension [57]). In particular this has to be addressed when it comes to numerical implementations of such models [58].

The CANNs used in our framework harbor - in addition to general mathematical laws of continuum mechanics - very little specific information, in fact only the pre-selection of a specific basis of generalized invariants. We tested two such bases (the one of the 4FF and the one of the GOH model) and found a similar

performance. It can indeed be assumed that the generalized invariant basis of any well-established constitutive equation would work because if that basis confined the functional space in a way that makes it *a priori* impossible to capture the mechanical behavior of the tissue, the resulting constitutive equation would suffer from such severe problems in practice that it would never get established on a broader scale in the scientific community. Therefore, we are confident that our framework is rather robust with respect to the specific choice of the generalized invariant basis of the CANNs.

The microstructure that defines the mechanical behavior of arteries changes substantially during maturation and aging. To understand how this affects the relevance of different microstructural features, we also performed a separate LRP for each age group. This analysis revealed a strong dependence on age that has to our knowledge not yet been reported so far. Specifically, our results reveal a trend towards greater relevance of the collagen volume fraction and recruitment and fiber straightness for age groups beyond the point of mechanical maturation, assumed for mice at an age of 56 days after birth [26]. In contrast, for age groups intermediate to maturation, there is instead a higher relevance of features related to major vascular cells in the tissue, consistent with the transition from a cell-dominated (early in development) to a balanced cell and matrix microstructure. Although still modest compared to the relevance of collagen parameters, the relevance of these parameters stands out at this age, which would be expected to be even more important prior to P21.

It is important to note that our studies, though promising, are not without several limitations. First, our study is limited to the elastic regime. A natural extension of interest would be the inelastic regime to include microstructural damage and ultimately rupture, which could help to improve risk assessments, for example, for aneurysms. In this regards, given our focus on healthy tissue herein, pathologies leading to aneurysms also affect the tissue microstructure and it is not clear at present to which extent our observations carry over to such states. Second, the employed microstructural descriptors were averaged over the dorsal and ventral sides of each aorta and were taken under age-specific diastolic loading conditions. Future studies should consider regional variations and local heterogeneities as well as loading-adapted descriptors in quantifying the relevance of the different microstructural features. Third, the collagen fiber architecture was assumed to have a planar distribution in the murine aorta, wherein all fiber orientations were mapped to the axial-circumferential plane. Future studies should aim at considering possible out-of-plane orientations whose importance has been noted for human tissue [59]. Thus, in future studies this information could be directly incorporated into the invariant basis of the CANNs. Lastly, it should be mentioned that the mechanical properties observed in soft tissue often depend on the mechanical testing protocol. Therefore, it is important to mention that the machine learning architecture trained as reported herein can make predictions that should in general only be used in a setting based on mechanical properties measured with similar mechanical testing protocols as used for the training data herein, which were biaxial under physiologic conditions while maintaining the native geometry, which tends to be more in vivo relevant that many other methods, including uniaxial testing and in-plane biaxial (in which natural residual stresses are relieved when preparing the samples). This limitation is true for most ML models, even though recent advances in the area of sensor fusing promises the potential of using data of different sources for a single trained ML model [60].

The framework we present in our paper is to our best knowledge at the moment the most accurate and best validated framework to predict macroscopic mechanical properties from microstructural information of soft tissue. At the same time, we also emphasize in the previous paragraph that this study should be viewed only as a first step and that further studies should be carried out with more data in order to better understand the strengths and limitations of our novel approach and to validate its predictive abilities on a broader data basis and thus in a statistically more reliable manner. Altogether, our study reveals that physics-informed machine learning can provide numerous insights into relations between microstructure and macroscopic mechanical properties in soft biological tissues. Such insights promise to impact precision medicine as well as advancing technologies, including regenerative medicine.

Declaration of Competing Interest

The authors declare that they have no known competing financial interests or personal relationships that could have appeared to influence the work reported in this paper.

Acknowledgments

This work was supported, in part, by grants from the US NIH (R01 HL105297, U01 HL142518).

Supplementary material

Supplementary material associated with this article can be found, in the online version, at doi:10.1016/j.actbio.2022.05.039.

References

[1] E.J. Topol, High-performance medicine: the convergence of human and artificial intelligence, Nat Med 25 (1) (2019) 44, doi:10.1038/s41591-018-0300-7.
[2] Y. Zhang, V.H. Barocas, S.A. Berceli, C.E. Clancy, D.M. Eckmann, M. Garbey, G.S. Kassab, D.R. Lochner, A.D. McCulloch, R. Tran-Son-Tay, et al., Multi-scale modeling of the cardiovascular system: disease development, progression, and clinical intervention, Annals of biomedical engineering 44 (9) (2016) 2642–2660.
[3] G.A. Holzapfel, R.W. Ogden, Biomechanical relevance of the microstructure in artery walls with a focus on passive and active components, American Journal of Physiology-Heart and Circulatory Physiology 315 (3) (2018) H540–H549.
[4] J.D. Humphrey, M.A. Schwartz, G. Tellides, D.M. Milewicz, Role of mechanotransduction in vascular biology: focus on thoracic aortic aneurysms and dissections, Circulation research 116 (8) (2015) 1448–1461.
[5] A. Tsamis, J.T. Krawiec, D.A. Vorp, Elastin and collagen fibre microstructure of the human aorta in ageing and disease: a review, Journal of the Royal Society Interface 10 (83) (2013) 20121004.
[6] E.G. Lakatta, M. Wang, S.S. Najjar, Arterial aging and subclinical arterial disease are fundamentally intertwined at macroscopic and molecular levels, Medical Clinics of North America 93 (3) (2009) 583–604.
[7] P. Hunter, N. Smith, J. Fernandez, M. Tawhai, Integration from proteins to organs: the IUPS physiome project, Mechanisms of ageing and development 126 (1) (2005) 187–192.
[8] J. Masison, J. Beezley, Y. Mei, H. Ribeiro, A.C. Knapp, L.S. Vieira, B. Adhikari, Y. Scindia, M. Grauer, B. Helba, et al., A modular computational framework for medical digital twins, Proceedings of the National Academy of Sciences 118 (20) (2021).
[9] A. Kaboudian, E.M. Cherry, F.H. Fenton, Real-time interactive simulations of large-scale systems on personal computers and cell phones: Toward patient-specific heart modeling and other applications, Science advances 5 (3) (2019) eaav6019.
[10] J.K. Shade, A. Prakosa, D.M. Popescu, R. Yu, D.R. Okada, J. Chrispin, N.A. Trayanova, Predicting risk of sudden cardiac death in patients with cardiac sarcoidosis using multimodality imaging and personalized heart modeling in a multivariable classifier, Science Advances 7 (31) (2021) eabi8020.
[11] H. Chen, Y. Liu, M.N. Slipchenko, X. Zhao, J.-X. Cheng, G.S. Kassab, The layered structure of coronary adventitia under mechanical load, Biophysical journal 101 (11) (2011) 2555–2562.
[12] M.-J. Chow, R. Turcotte, C.P. Lin, Y. Zhang, Arterial extracellular matrix: a mechanobiological study of the contributions and interactions of elastin and collagen, Biophysical journal 106 (12) (2014) 2684–2692.
[13] S. Sugita, T. Matsumoto, Multiphoton microscopy observations of 3d elastin and collagen fiber microstructure changes during pressurization in aortic media, Biomechanics and modeling in mechanobiology 16 (3) (2017) 763–773.
[14] W. Krasny, H. Magoariec, C. Morin, S. Avril, Kinematics of collagen fibers in carotid arteries under tension-inflation loading, Journal of the mechanical behavior of biomedical materials 77 (2018) 718–726.

[15] C. Cavinato, P. Badel, W. Krasny, S. Avril, C. Morin, Experimental characterization of adventitial collagen fiber kinematics using second-harmonic generation imaging microscopy: similarities and differences across arteries, species and testing conditions, in: Multi-scale Extracellular Matrix Mechanics and Mechanobiology, Springer, 2020, pp. 123–164.
[16] C. Cavinato, S.-I. Murtada, A. Rojas, J.D. Humphrey, Evolving structure-function relations during aortic maturation and aging revealed by multiphoton microscopy, Mechanisms of Ageing and Development 196 (2021) 111471.
[17] X. Yu, R. Turcotte, F. Seta, Y. Zhang, Micromechanics of elastic lamellae: unravelling the role of structural inhomogeneity in multi-scale arterial mechanics, Journal of The Royal Society Interface 15 (147) (2018) 20180492.
[18] B. Spronck, R.T.A. Megens, K.D. Reesink, T. Delhaas, A method for three-dimensional quantification of vascular smooth muscle orientation: application in viable murine carotid arteries, Biomechanics and modeling in mechanobiology 15 (2) (2016) 419–432.
[19] J.A. Niestrawska, C. Viertler, P. Regitnig, T.U. Cohnert, G. Sommer, G.A. Holzapfel, Microstructure and mechanics of healthy and aneurysmatic abdominal aortas: experimental analysis and modelling, Journal of The Royal Society Interface 13 (124) (2016) 20160620.
[20] M. Amabili, M. Asgari, I.D. Breslavsky, G. Franchini, F. Giovanniello, G.A. Holzapfel, Microstructural and mechanical characterization of the layers of human descending thoracic aortas, Acta Biomaterialia (2021).
[21] M.R. Hill, X. Duan, G.A. Gibson, S. Watkins, A.M. Robertson, A theoretical and non-destructive experimental approach for direct inclusion of measured collagen orientation and recruitment into mechanical models of the artery wall, Journal of biomechanics 45 (5) (2012) 762–771.
[22] W. Wan, J.B. Dixon, R.L. Gleason Jr, Constitutive modeling of mouse carotid arteries using experimentally measured microstructural parameters, Biophysical journal 102 (12) (2012) 2916–2925.
[23] R. Rezakhaniha, E. Fonck, C. Genoud, N. Stergiopulos, Role of elastin anisotropy in structural strain energy functions of arterial tissue, Biomechanics and modeling in mechanobiology 10 (4) (2011) 599–611.
[24] Y. Wang, S. Zeinali-Davarani, Y. Zhang, Arterial mechanics considering the structural and mechanical contributions of ECM constituents, Journal of biomechanics 49 (12) (2016) 2358–2365.
[25] J.E. Wagenseil, R.P. Mecham, Vascular extracellular matrix and arterial mechanics, Physiological reviews 89 (3) (2009) 957–989.
[26] S.-I. Murtada, Y. Kawamura, G. Li, M.A. Schwartz, G. Tellides, J.D. Humphrey, Developmental origins of mechanical homeostasis in the aorta, Developmental Dynamics 250 (5) (2021) 629–639.
[27] J. Ferruzzi, D. Madziva, A.W. Caulk, G. Tellides, J.D. Humphrey, Compromised mechanical homeostasis in arterial aging and associated cardiovascular consequences, Biomechanics and modeling in mechanobiology 17 (5) (2018) 1281–1295.
[28] J.Z. Hawes, A.J. Cocciolone, A.H. Cui, D.B. Griffin, M.C. Staiculescu, R.P. Mecham, J.E. Wagenseil, Elastin haploinsufficiency in mice has divergent effects on arterial remodeling with aging depending on sex, American Journal of Physiology–Heart and Circulatory Physiology 319 (6) (2020) H1398–H1408.
[29] N. Choudhury, O. Bouchot, L. Rouleau, D. Tremblay, R. Cartier, J. Butany, R. Mongrain, R.L. Leask, Local mechanical and structural properties of healthy and diseased human ascending aorta tissue, Cardiovascular Pathology 18 (2) (2009) 83–91.
[30] S. Sherifova, G. Sommer, C. Viertler, P. Regitnig, T. Caranasos, M.A. Smith, B.E. Griffith, R.W. Ogden, G.A. Holzapfel, Failure properties and microstructure of healthy and aneurysmatic human thoracic aortas subjected to uniaxial extension with a focus on the media, Acta biomaterialia 99 (2019) 443–456.
[31] J. Ferruzzi, M.R. Bersi, S. Uman, H. Yanagisawa, J.D. Humphrey, Decreased elastic energy storage, not increased material stiffness, characterizes central artery dysfunction in fibulin-5 deficiency independent of sex, Journal of biomechanical engineering 137 (3) (2015) 031007.
[32] M.R. Bersi, R. Khosravi, A.J. Wujciak, D.G. Harrison, J.D. Humphrey, Differential cell-matrix mechanoadaptations and inflammation drive regional propensities to aortic fibrosis, aneurysm or dissection in hypertension, Journal of The Royal Society Interface 14 (136) (2017) 20170327.
[33] Y. Kawamura, S.-I. Murtada, F. Gao, X. Liu, G. Tellides, J.D. Humphrey, Adventitial remodeling protects against aortic rupture following late smooth muscle-specific disruption of TGFβ signaling, Journal of the Mechanical Behavior of Biomedical Materials 116 (2021) 104264.
[34] M. Mozaffar, R. Bostanabad, W. Chen, K. Ehmann, J. Cao, M.A. Bessa, Deep learning predicts path-dependent plasticity, Proceedings of the National Academy of Sciences 116 (52) (2019) 26414–26420.
[35] K. Linka, M. Hillgärtner, K.P. Abdolazizi, R.C. Aydin, M. Itskov, C.J. Cyron, Constitutive artificial neural networks: A fast and general approach to predictive data-driven constitutive modeling by deep learning, J Comput Phys 429 (2021) 110010, doi:10.1016/j.jcp.2020.110010.
[36] M. Raissi, P. Perdikaris, G.E. Karniadakis, Physics-informed neural networks: A deep learning framework for solving forward and inverse problems involving nonlinear partial differential equations, Journal of Computational Physics 378 (2019) 686–707.
[37] G.C.Y. Peng, M. Alber, A.B. Tepole, W.R. Cannon, S. De, S. Dura-Bernal, K. Garikipati, G. Karniadakis, W.W. Lytton, P. Perdikaris, et al., Multiscale modeling meets machine learning: What can we learn? Archives of Computational Methods in Engineering 28 (3) (2021) 1017–1037.
[38] F. Sahli Costabal, Y. Yang, P. Perdikaris, D.E. Hurtado, E. Kuhl, Physics-informed neural networks for cardiac activation mapping, Frontiers in Physics 8 (2020) 42.
[39] K. Linka, N. Reiter, J. Würges, M. Schicht, L. Bräuer, C.J. Cyron, F. Paulsen, S. Budday, Unraveling the local relation between tissue composition and human brain mechanics through machine learning, Frontiers in bioengineering and biotechnology (2021) 712.
[40] G.A. Holzapfel, K. Linka, S. Sherifova, C.J. Cyron, Predictive constitutive modelling of arteries by deep learning, Journal of the Royal Society Interface 18 (182) (2021) 20210411.
[41] S. Bach, A. Binder, G. Montavon, F. Klauschen, K.-R. Müller, W. Samek, On pixel-wise explanations for non-linear classifier decisions by layer-wise relevance propagation, PloS one 10 (7) (2015) e0130140, doi:10.1371/journal.pone.0130140.
[42] J.D. Humphrey, Cardiovascular solid mechanics: cells, tissues, and organs, Springer Science & Business Media, 2013.
[43] S.R. Jammalamadaka, A. Sengupta, Topics in circular statistics, volume 5, world scientific, 2001.
[44] T.C. Gasser, R.W. Ogden, G.A. Holzapfel, Hyperelastic modelling of arterial layers with distributed collagen fibre orientations, Journal of the royal society interface 3 (6) (2006) 15–35.
[45] F. Schroeder, S. Polzer, M. Slažanskỳ, V. Man, P. Skácel, Predictive capabilities of various constitutive models for arterial tissue, Journal of the mechanical behavior of biomedical materials 78 (2018) 369–380.
[46] D.P. Kingma, J. Ba, Adam: A method for stochastic optimization, in: Proceedings of the 3rdInternational Conference on Learning Representations (ICLR), volume 5, 2015.
[47] F. Chollet, Keras, 2015, (https://github.com/fchollet/keras).
[48] M. Abadi, A. Agarwal, P. Barham, E. Brevdo, Z. Chen, C. Citro, G. Corrado, A. Davis, J. Dean, M. Devin, S. Ghemawat, I. Goodfellow, A. Harp, G. Irving, M. Isard, Y. Jia, R. Jozefowicz, L. Kaiser, M. Kudlur, J. Levenberg, D. Mané, R. Monga, S. Moore, D. Murray, C. Olah, M. Schuster, J. Shlens, B. Steiner, I. Sutskever, K. Talwar, P. Tucker, V. Vanhoucke, V. Vasudevan, F. Viégas, O. Vinyals, P. Warden, M. Wattenberg, M. Wicke, Y. Yu, X. Zheng, TensorFlow: Large-scale machine learning on heterogeneous systems, 2015,. Software available from tensorflow.org, https://www.tensorflow.org/.
[49] J.D. Humphrey, G.A. Holzapfel, Mechanics, mechanobiology, and modeling of human abdominal aorta and aneurysms, Journal of biomechanics 45 (5) (2012) 805–814.
[50] H. Weisbecker, M.J. Unterberger, G.A. Holzapfel, Constitutive modelling of arteries considering fibre recruitment and three-dimensional fibre distribution, Journal of The Royal Society Interface 12 (105) (2015) 20150111.
[51] P.N. Watton, N.A. Hill, Evolving mechanical properties of a model of abdominal aortic aneurysm, Biomechanics and modeling in mechanobiology 8 (1) (2009) 25–42.
[52] A. Hamedzadeh, T.C. Gasser, S. Federico, On the constitutive modelling of recruitment and damage of collagen fibres in soft biological tissues, European Journal of Mechanics-A/Solids 72 (2018) 483–496.
[53] A. Gizzi, M. Vasta, A. Pandolfi, Modeling collagen recruitment in hyperelastic bio-material models with statistical distribution of the fiber orientation, International Journal of Engineering Science 78 (2014) 48–60.
[54] J.D. Humphrey, R.K. Strumpf, F.C.P. Yin, Determination of a Constitutive Relation for Passive Myocardium: I. A New Functional Form, Journal of Biomechanical Engineering 112 (3) (1990) 333–339, doi:10.1115/1.2891193. https://asmedigitalcollection.asme.org/biomechanical/article-pdf/112/3/333/5531142/333_1.pdf.
[55] J.D. Humphrey, R.K. Strumpf, F.C.P. Yin, Determination of a Constitutive Relation for Passive Myocardium: II.'Parameter Estimation, Journal of Biomechanical Engineering 112 (3) (1990) 340–346, doi:10.1115/1.2891194. https://asmedigitalcollection.asme.org/biomechanical/article-pdf/112/3/340/5531261/340_1.pdf.
[56] G. Martufi, T.C. Gasser, Turnover of fibrillar collagen in soft biological tissue with application to the expansion of abdominal aortic aneurysms, Journal of The Royal Society Interface 9 (77) (2012) 3366–3377, doi:10.1098/rsif.2012.0416.
[57] P. Skacel, J. Bursa, Poissons ratio of arterial wall–inconsistency of constitutive models with experimental data, Journal of the mechanical behavior of biomedical materials 54 (2016) 316–327.
[58] J. Helfenstein, M. Jabareen, E. Mazza, S. Govindjee, On non-physical response in models for fiber-reinforced hyperelastic materials, International Journal of Solids and Structures 47 (16) (2010) 2056–2061.
[59] G.A. Holzapfel, J.A. Niestrawska, R.W. Ogden, A.J. Reinisch, A.J. Schriefl, Modelling non-symmetric collagen fibre dispersion in arterial walls, J R Soc Interface 12 (2015) 20150188, doi:10.1098/rsif.2015.0188.
[60] C. Ritter, T. Wollmann, J.-Y. Lee, A. Imle, B. Müller, O.T. Fackler, R. Bartenschlager, K. Rohr, Data fusion and smoothing for probabilistic tracking of viral structures in fluorescence microscopy images, Medical Image Analysis 73 (2021) 102168.